

Phase Regulation Promotes High Rate-Long Term $\text{Na}_4\text{Fe}_3(\text{PO}_4)_2\text{P}_2\text{O}_7$ Cathode for Sodium-Ion Batteries

Haiyan Yang,^[a] Xinhai Li,^[a, b, c] Zhixing Wang,^[a, b, c] Huajun Guo,^[a, b, c] Hui Duan,^[a, b, c] Jiexi Wang,^[a, b, c] Guangchao Li,^{*[a, b, c]} and Guochun Yan^{*[a, b, c]}

Sodium-ion batteries (SIBs) have evoked much attention, benefiting from the advantages of low cost, high safety and excellent performance at low temperature. Especially, $\text{Na}_4\text{Fe}_3(\text{PO}_4)_2\text{P}_2\text{O}_7$ (NFPP) cathode is considered to be one of the best candidates for SIBs cathode with abundant resources and long-term cycling stability. However, the impurities of NaFePO_4 (NFP) and $\text{Na}_2\text{FeP}_2\text{O}_7$ (NFPO) formed synchronously with NFPP which restrict the further application of NFPP. It is meaningful to clear the formation process and regulate the contents of NFP and NFPO. Therefore, NFPP cathodes with different contents of NFP and NFPO were prepared through high energy ball milling

cooperated with post-heat treatment by controlling the Fe concentration in reactants. The NFPP-2.85 showed the best electrochemical performance because of the high content of NFPP and transition zone between NFPP and NFPO which fasts the Na^+ transport kinetics. When employed as cathode for SIBs, the as-prepared NFPP-2.85 showed a specific capacity of 111.8 mAh g^{-1} at 0.1 C and maintained at 68.9 mAh g^{-1} even at 100 C. The retention ratio was as high as 93.6% after 1500 cycles at 20 C, implying superior high rate-long term cycling stability. This work provides a new way for impurities regulation and the improvement of NFPP electrochemical performance.

Introduction

Recently, the development and utilization of renewable energy have become more and more interesting, including solar energy, wind energy, hydro energy and biomass energy, etc, inspiring the demand for high efficient energy storage systems (ESSs).^[1] Among the various ESSs, electrochemical energy storage and conversion devices possess the advantages of high response sensitivity, high energy density and environmental friendliness.^[2] Especially, sodium-ion batteries (SIBs) are considered to be one of the best choices for ESSs, benefiting from the merits of low cost and superior electrochemical performance in extreme environment.^[3] However, the unsatisfying cathode materials restrict their further development of SIBs, taking the high specific capacity, excellent rate performance and long-term cycling stability into considerations. For example, layered cathode of SIBs delivers high specific capacity, but the structural aberration and interfacial degradation result in poor cycling life.^[4] Besides that, the dissolution of transition metal ions and high hydrate contents of Prussian Blue/White analogs contrib-

ute to poor structural stability, manifesting inferior electrochemical property.^[5]

As a comparison, polyanion compounds deliver stable structure, high working voltage, superior thermal stability and long-term cycling life, making them favorable electrode materials for ESSs, especially $\text{Na}_4\text{M}_3(\text{PO}_4)_2\text{P}_2\text{O}_7$ ($\text{M}=\text{Mn, Fe, Co, Ni}$).^[6] Whereas, the low electronic conductivity, relatively high cost and complex impurities limit the commercial process.^[7] The conductivity can be largely improved by carbon coating, particle sizes controlling and hetero-atoms doping.^[8] Moreover, the cost is controllable by changing the Co, Ni to Mn, Fe.^[9] The main challenge is that the high purity phase is hard to be achieved.^[7c,10] As an example, the maricite orthophosphate (NaFePO_4 , NFP) and pyrophosphate ($\text{Na}_2\text{FeP}_2\text{O}_7$, NFPO) are the impurities for $\text{Na}_4\text{Fe}_3(\text{PO}_4)_2\text{P}_2\text{O}_7$ (NFPP).^[6d,11] It has been proven to be that iron-rich state is beneficial for the formation of NFP, while NFPO is assigned to the iron-poor state.^[11e,f,12] It is very meaningful to reveal the regulation rule for NFP and NFPO phases which can guide us to prepare high purity NFPP materials. In this way, the electrochemical performance can be easily promoted. For example, Cao et al. reported that owing to the presence of NFP impurity with electrochemical inert, the high capacity of NFPP is greatly restricted.^[11d] Fortunately, they found that a very clean single phase of NFPP was successfully achieved by inducing 3% of Fe vacancy defects, which demonstrated the high capacity of 110.9 mAh g^{-1} at 0.2 C. In addition, Fei et al. discovered Ni-substituting was conducive to inhibiting electrochemical inert maricite-NFP impurity and enhance the Na^+ diffusion kinetics.^[13] It is found that the optimal $\text{Na}_4\text{Fe}_{2.82}\text{Ni}_{0.18}(\text{PO}_4)_2\text{P}_2\text{O}_7$ cathode showed superior electrochemical performance in terms of high reversible capacity (128 mAh g^{-1} at 0.2 C), outstanding cycle stability (capacity retention of ~83% after 3000 cycles at 10 C) and rate performance (62.5 mAh g^{-1} at 50 C). As for NFPO impurity, although

[a] H. Yang, X. Li, Z. Wang, H. Guo, H. Duan, J. Wang, G. Li, G. Yan
School of Metallurgy and Environment, Central South University, Changsha, Hunan 410083, China
E-mail: guangchao_li@csu.edu.cn
happyycg@csu.edu.cn

[b] X. Li, Z. Wang, H. Guo, H. Duan, J. Wang, G. Li, G. Yan
National Energy Metal Resources and New Materials Key Laboratory, Central South University, Changsha 410083, China

[c] X. Li, Z. Wang, H. Guo, H. Duan, J. Wang, G. Li, G. Yan
National Engineering Research Centre of Advanced Energy Storage Materials, Changsha, Hunan 410083, China

 Supporting information for this article is available on the WWW under <https://doi.org/10.1002/batt.202400438>

owning a tree-dimensional framework for Na^+ migration, its theoretical capacity is relatively low.^[14] As expected, the presence of NFPO impurity have an unfavorable impact on the NFPP electrochemical performance in the matter of reversible capacity and voltage plateaus.^[11f] Therefore, Zhang et al. used the Fe-sites V generation to reduce the formation NFPO in NFPP.^[15] The $\text{Na}_{3.94}\text{Fe}_{2.94}\text{P}_{0.06}(\text{PO}_4)_2\text{P}_2\text{O}_7$ cathode obtained displayed high specific capacity of 128 mAhg^{-1} and excellent long term with capacity retention of 81.65% after 10,000 cycles at 20 C. Taking the above illustrations into accounts, the regulation of NFP and NFPO impurities makes significant scene to the electrochemical performance of NFPP. It is of interesting to clear the phase regulation and transformation mechanism during the formation of NFPP cathode.

Herein, NFPP cathode with different contents of NFP and NFPO were prepared through high energy ball milling cooperated with post-heat treatment. In this way, the formation rule of NFP and NFPO was clearly revealed. The low Fe concentration was beneficial to the formation of NFP while high Fe concentration was devoted to NFPO. The NFPP content reached 92.8% with a certain amount of NFPO impurity by regulating the Fe concentration. When employed as cathode for SIBs, the as-prepared NFPP-2.85 showed a specific capacity of 111.8 mAhg^{-1} at 0.1 C and the specific capacity maintained at 68.9 mAhg^{-1} even at 100 C. The retention ratio was as high as 93.6% after 1500 cycles at 20 C, implying superior high rate-long term cycling stability.

Results and Discussion

As shown in Figure S1, the NFPP-x ($x=3.00, 2.90, 2.85, 2.70$) materials were prepared in a typical high energy ball milling cooperated with heat treatment. Typically, a certain amount of NaH_2PO_4 , $\text{FeC}_2\text{O}_4 \cdot 2\text{H}_2\text{O}$ and Ketjen Black (KB) were mixed and uniformly distributed under the effect of high energy ball milling. After that, the as-obtained precursor was heated in a tube furnace to obtain final NFPP materials. The impurities can be readily controlled by regulating the addition of $\text{FeC}_2\text{O}_4 \cdot 2\text{H}_2\text{O}$ content. It can be seen from Figure 1a that the diffraction peaks of the as-prepared samples are associated to the NFPP (PDF card No.89-0579), belonging to $Pn2_1a$ space group with the orthogonal structure. Moreover, there are still some impurities located at $2\theta = \sim 32.8^\circ$ and $\sim 33.8^\circ$ which are assigned to maricite-NFP (PDF card No.29-1296) and NFPO (PDF card No.80-2409) phases, individually. To confirm the contents of impurities, Rietveld refinement is performed, as shown in Figure 1b-f. The corresponding phase composition and crystallographic parameter are summarized in Tables S1-S3. The calculated NFP contents in NFPP-3.00 and NFPP-2.90 are 10.7% and 5.6%, while NFPP purity increases with the decrease of Fe concentration in reactant. As for the NFPO impurity, the calculated values are 7.2% and 20.2% in NFPP-2.85 and NFPP-2.70. It can be seen from the XRD results that the formation of NFP and NFPO is related to the local Fe concentration. The higher Fe concentration is, the higher NFP is and low Fe concentration is

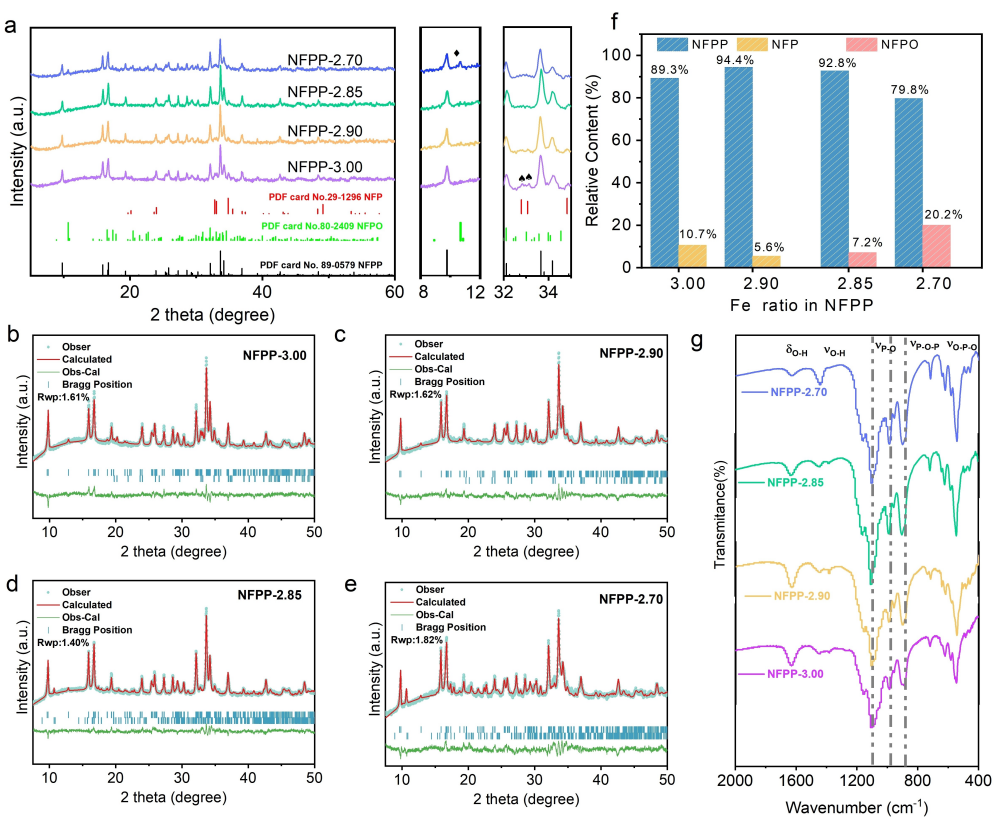


Figure 1. Structural characterization of the as-prepared NFPP samples. (a) XRD, (b–e) Rietveld refined results of NFPP-3.00, NFPP-2.90, NFPP-2.85 and NFPP-2.7, (f) Phase contents analysis, (g) FT-IR results.

benefit to the formation of NFPO. The NFPP content can reach as high as 94.4% by regulating the Fe concentration. Further, the cell volume increases with the improvement of NFPP contents which is beneficial for the transportation of Na^+ .

As for the FT-IR results in Figure 1g, the peaks center at $400\text{--}620\text{ cm}^{-1}$ and $950\text{--}1300\text{ cm}^{-1}$ are attributed to the bending vibration of O-P-O and stretching vibration of P-O of PO_4^{3-} . While the peak around $710\text{--}905\text{ cm}^{-1}$ belongs to the stretch and vibration of symmetric and asymmetric P-O-P of $\text{P}_2\text{O}_7^{4-}$ ^[16]. Especially, the signals of PO_4^{3-} and $\text{P}_2\text{O}_7^{4-}$ can be detected among all the samples. It should be noted that the peaks locate at 716 cm^{-1} and 884.9 cm^{-1} gradually shift to left with the decrease of Fe concentration, indicating that the $\text{P}_2\text{O}_7^{4-}$ feature is stronger. The above results demonstrate that the amount and location of PO_4^{3-} and $\text{P}_2\text{O}_7^{4-}$ probably vary from different NFPP materials, which may give rise to the change of structure stability. It is likely to be favorable for Na^+ transportation channel by replacing PO_4^{3-} polyanion unit with $\text{P}_2\text{O}_7^{4-}$ ^[17].

The microtopography information is determined by SEM and TEM investigations. It can be seen from Figures S2–S3 that the as-prepared samples exhibit similar shape and size with irregular bulk structure. The floccules around particles can be ascribed to the introduced carbon. When it comes to the TEM images in Figure 2a–d, NFPP with different lattice plane can be found in various NFPP materials which act as the main constituent of the samples. The crystal structure of NFPP is formed if three FeO_6 octahedra meets three PO_4 tetrahedra along b and c axes to form an infinite $[\text{Fe}_3\text{P}_2\text{O}_{13}]$ unit lamellar structure. However, FeO_6 octahedral tend to connect with each other and form an infinite layer along the b-axis to form the impurity of NFP when the local accumulation of iron (Fe) concentration occurs in the sintering process. Otherwise, if the local Fe concentration is insufficient, the FeO_6 arrangement orientation will be changed and thus results in the formation of two FeO_6 octahedra and two PO_4 tetrahedra arranged along b and c axes, respectively. In this way, NFPO impurity forms. Besides that, carbon coating layer also find around the outside of the bulk. Especially, the interlayer of 0.273 nm in Figure 2a is assigned to the (220) plane of NFP, implying the impurity appearances. Whereas, it can not be detected because of the relatively low content which has decreased from 10.7% in NFPP-3.00 to 5.6% in NFPP-2.90. With the increase of Fe content in reactant, the impurity changes from NFP to NFPO, which can be clearly concluded from NFPP-2.85 and NFPP-2.70. Similar results are also revealed by SAED tests (Figures S4–S5). As for the elements distribution in NFPP samples (Figures 2e and S6), Na, P, O and Fe are distributed uniformly in the as-prepared materials. Based on the above results, it is estimated that the generation of NFP and NFPO impurities is probably attributed to the variations in growth direction for a structural framework that resulted from inhomogeneous Fe diffusion concentration during the synthesis process. Besides, it is noted that there is a transitional zone between NFPP crystal and NFPO, which is likely to have an influence on material structure, especially as regard to the sodium transfer channels.

The Raman Spectroscopy was used to investigate the materials structure, as shown in Figure 3a. D band and G band are detected, which are related to carbon precipitated. The relative intensity of I_D/I_G usually evaluates the degree of graphitization of carbon, and the I_D/I_G values of all sample are nearly similar, indicating that the similar graphitization degree in the materials. Figure 3b–d is the characterization of the NFPP

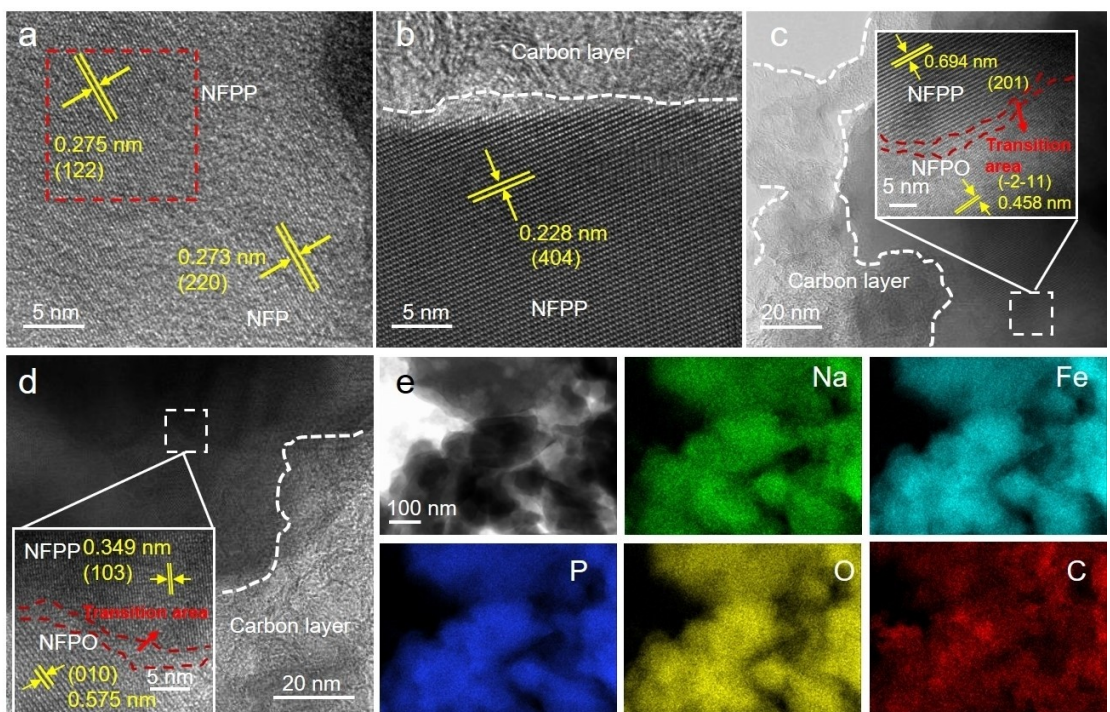


Figure 2. TEM and elements distribution of NFPP samples. (a) NFPP-3.00, (b) NFPP-2.90, (c) NFPP-2.85, (d) NFPP-2.70, (e) EDS mapping results of NFPP-2.85.

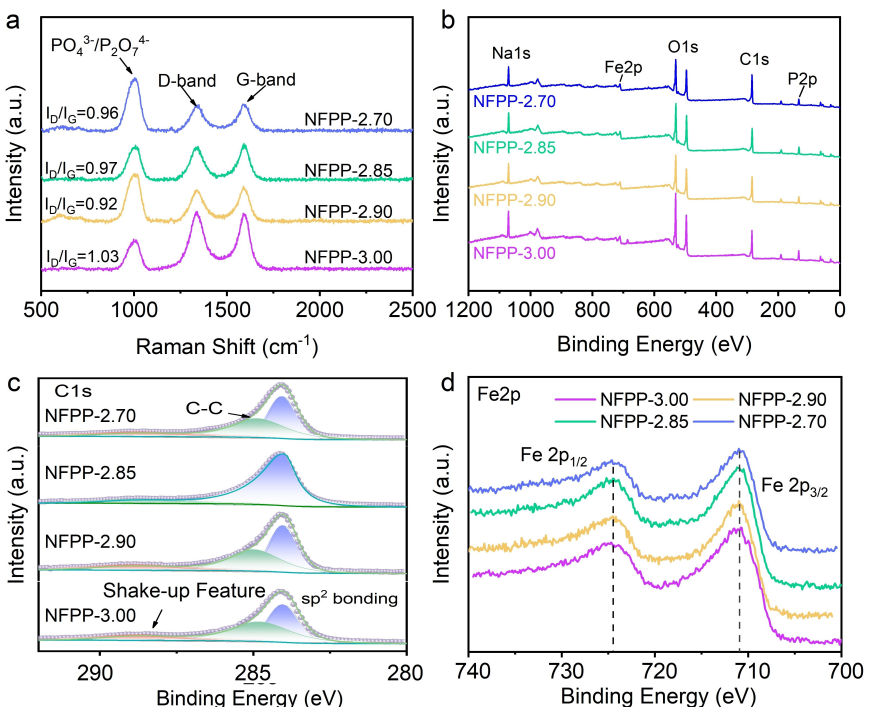


Figure 3. Structural information of NFPP samples. (a) Raman spectra, (b) XPS survey spectra and corresponding high-resolution spectrum of (c) C 1s, (d) Fe 2p.

materials by X-ray photoelectron spectroscopy (XPS). A wide range of full survey-P–Fe–O diagram is displayed in Figure 3b. The high-resolution C 1s peak can be found in 284.8 eV and 284 eV which belongs to the interaction of C–C bonds and sp² carbon species, implying the existence of KB (as shown in Figure 3c). Besides that, Figure 3d reveals that the Fe 2p_{1/2} and Fe 2p_{3/2} are roughly 724.5 eV and 710.8 eV, respectively, which indicates that the presence of Fe element in terms of Fe²⁺ in all samples. The detailed carbon contents are further confirmed by TG analysis, as shown in Figure S7. And the calculated values are listed in Table S4. The weight loss of NFPP-3.00, NFPP-2.90, NFPP-2.85 and NFPP-2.70 is 2.91, 3.13, 3.17 and 3.85%, revealing the carbon contents are 6.50, 6.71, 6.75 and 7.14%, respectively. The coating carbon is conductive to the electrons transfer and thus long-term cycling performance is promoted especially under high rate.

To further confirm the effects of NFP and NFPO impurities on the NFPP electrochemical performance, the as-prepared samples are assembled as half cells and full cells. It can be seen from Figure 4a that three redox-reduction pairs are detected in all NFPP samples which are assigned to the Na⁺ de-interaction/interaction at different stage. Moreover, oxidized peaks around 2.5 V appear in NFPP-2.85 and NFPP-2.70, confirming the existence of NFPO impurity again.^[18] Similar peaks cannot be found in NFPP-3.00 and NFPP-2.90 because NFP impurity is electrochemical inactivity. As for the charge-discharge profiles in Figure 4b, NFPP-3.00, NFPP-2.90, NFPP-2.85 and NFPP-2.70 deliver specific capacity of 101.5, 104.6, 111.8 and 103.5 mAh g⁻¹ at 0.1 C with coulombic efficiencies of 99.5, 100, 99.4 and 99.3%, respectively. NFPP-2.85 sample exhibit the

highest value than others because of the high pure NFPP exists. Rate performance show that all samples demonstrate superior rate capacity (Figures 4c and S8). In special, NFPP-2.85 delivers the best performance with a specific capacity as high as 68.9 mAh g⁻¹ even at 100 C which is much better than other samples. The superior rate performance might be attributed to the relatively low resistance (Figure S9 and Table S6). Moreover, the Na⁺ transport kinetic behavior is studied through GITT test, as shown in Figure 4d and Table S7. When compared to NFPP-3.00, NFPP-2.90 and NFPP-2.70, NFPP-2.85 delivers the highest Na⁺ diffusion coefficients, benefiting to the improvement of fast ions transport. Figure 4e presents the long cycling stability at 1 C. The reversible capacities of NFPP-3.00, NFPP-2.90, NFPP-2.85 and NFPP-2.70 are 94.6, 98.8, 105.9 and 99.4 mAh g⁻¹ at the first cycles, respectively, which retain 87.0, 92.6, 100.8 and 92.8 mAh g⁻¹ at the 500th cycles, respectively. The capacity retentions maintain at 91.9, 93.7, 95.1 and 93.7% after 500 cycles for NFPP-3.00, NFPP-2.90, NFPP-2.70 and NFPP-2.85, respectively. Moreover, NFPP-2.85 also delivers the highest capacity performance. Taking the above illustrations into conclusion, NFPP-2.85 shows high specific capacity, superior rate performance and long-term cycling performance by regulating the phase constituents of NFPP samples. The transition area of NFPP and NFPO can provide new Na⁺ diffusion channels which is beneficial for fast Na⁺ transfer and thus contributes to improved electrochemical performance. Besides that, the long-term cycling stability under ultra-high rate is also evaluated, as shown in Figure 5. The initial specific capacity reaches 94.3 mAh g⁻¹ at the current density of 20 C

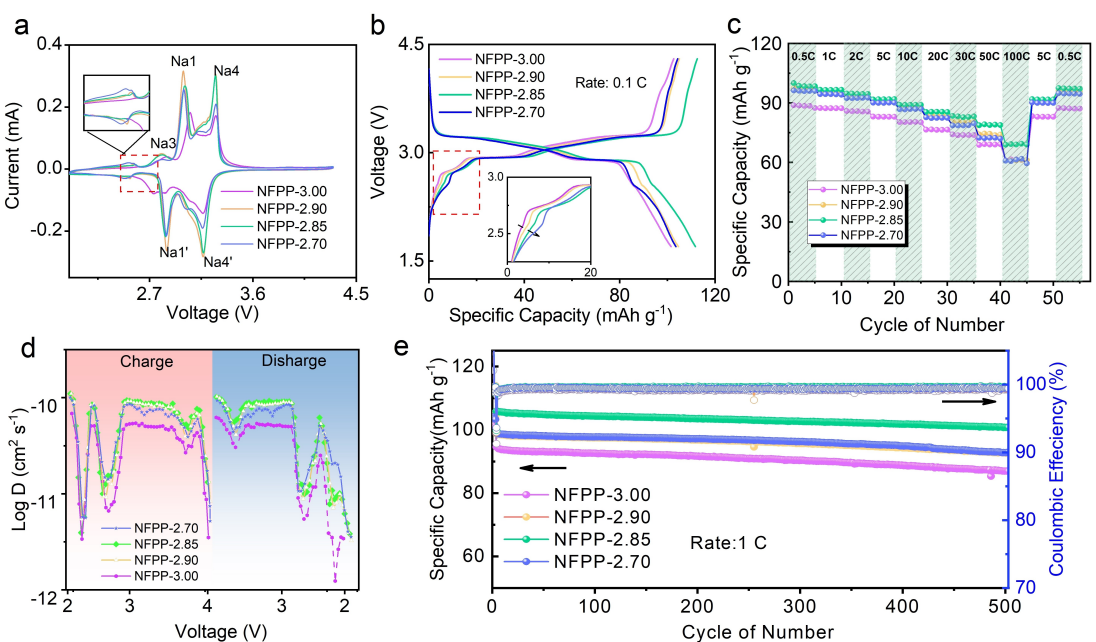


Figure 4. Electrochemical performance analysis of NFPP samples in half cells. (a) CV, (b) Charge/discharge profiles at 0.1 C, (c) Rate test, (d) GITT result; (e) Cycling performance at 1 C.

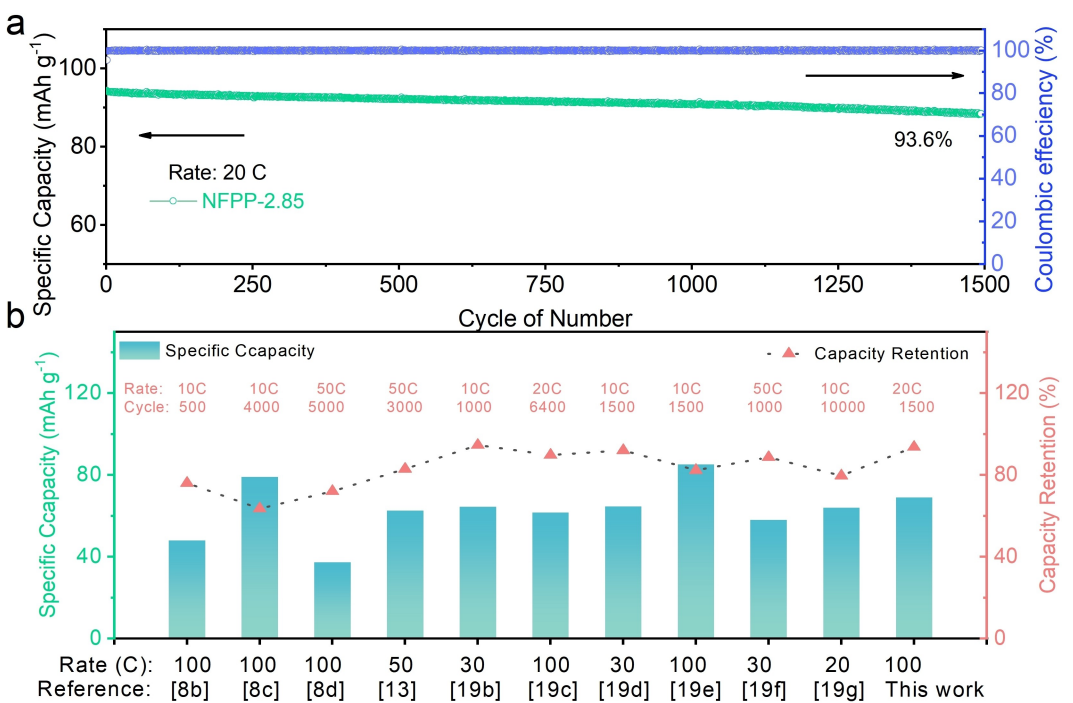


Figure 5. Cycling performance and comparisons with literatures. (a) Long-term cycling stability of NFPP sample at 20 C, (b) Comparisons with recent publications.

and maintains at 93.6% after 1500 cycles which is much better than recent published literatures.^[8b,c,e,13,19]

The coin full cell is prepared by employing NFPP cathode and commercial hard carbon (HC) anode. The ratio between anode and positive is set as 1.08~1.12. As shown in Figure 6a, the initial discharge capacity of the full cell can reach 89.2 mAh g^{-1} with columbic efficiency of 84.4%. After cycling

200 cycles at 0.5 C, the capacity keeps at 61.6 mAh g^{-1} with a capacity retention of 69.7%, demonstrating a potential application for commercial SIBs (Figure 6b).

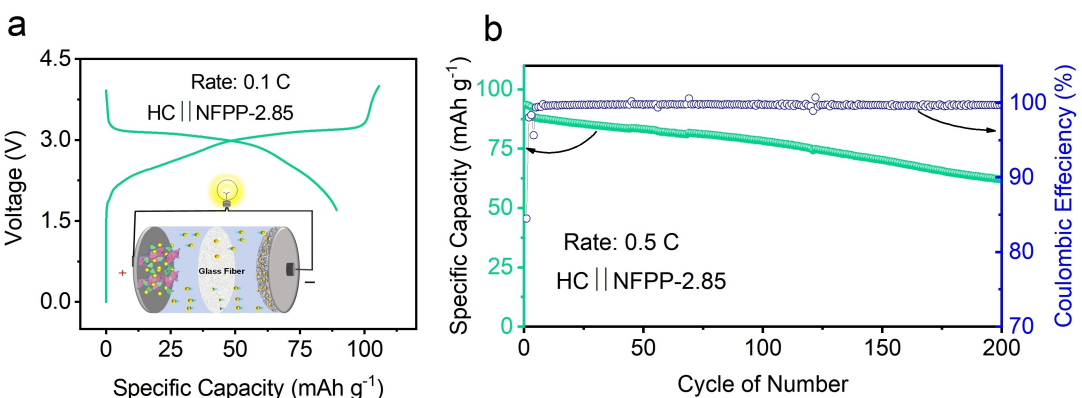


Figure 6. Full cell performance of HC || NFPP. (a) Charge/discharge profiles, (b) Cycling performance at 0.5 C for 200 cycles.

Conclusions

In summary, $\text{Na}_4\text{Fe}_3(\text{PO}_4)_2\text{P}_2\text{O}_7$, an iron-based mixed phosphate material with NASICON structure, was effectively synthesized by high-energy ball milling associated with heat treatment. The formation rule of NFP and NFPO impurities were systematically studied as well as their effects on electrochemical performance. Moreover, a certain amount of transition zone between NFPP and NFPO was benefit to the Na^+ transport kinetics. High specific capacity as high as 111.8 mAh g^{-1} was observed at 0.1 C for NFPP-2.85 and the capacity maintained at 68.9 mAh g^{-1} even tested at 100 C, implying superior rate capability. The capacity retention ratio reached 95.1% after 500 cycles at 1 C. Most importantly, it can keep at 93.6% even tested at 20 C for 1500 cycles, revealing excellent long-term cycling stability. All in all, NFPP cathode with high pure and superior rate performance was successfully made in a facial way which give a new method for impurities regulation and electrochemical performance improvement.

Experimental Section

Materials Preparation

All the chemicals in this paper were purchased from commercial suppliers and used without any further treatment. Especially, NaH_2PO_4 and $\text{FeC}_2\text{O}_4 \cdot 2\text{H}_2\text{O}$ were bought from Mackin reagent. $\text{CH}_3\text{CH}_2\text{OH}$ was provided by Tianjin Hengxing Chemical Preparation Co.ltd. The specification of conductive carbon Ketjen Black (KB) is ECP 600JD. In a typical ball milling process, 5.62 g NaH_2PO_4 (20 mmol) and 2.59 g $\text{FeC}_2\text{O}_4 \cdot 2\text{H}_2\text{O}$ (14.25 mmol) were employed as reactants and 0.16 g KB was added to improve the conductivity with the exist of $\text{CH}_3\text{CH}_2\text{OH}$ (30 mL) dispersive agent. All reactants were put in a ball mill tank (MITR YXQM-250 ml, Changsha Miqi Instrument and Equipment Co., Ltd.) where the air was washed out by argon gas. The mixing process was treated with planetary ball mill machine with a 5 minute pause in every 30 min and the mass ratio of powder to balls is controlled at about 1:25. After high energy ball milling for 4 h at 500 rpm, the mixture was dried at 80 °C for 8 h in a vacuum oven. Subsequently, the dried precursor was transferred into a tube furnace and sintering at 450 °C with the heating rate of 5°C min^{-1} for 10 h in a high-purity argon atmosphere. The product was collected after cooling down to room

temperature and named as NFPP-2.85. Similarly, NFPP-3.00, NFPP-2.90 and NFPP-2.70 were prepared by changing the contents of $\text{FeC}_2\text{O}_4 \cdot 2\text{H}_2\text{O}$ to 15.0, 14.5 and 13.5 mmol.

Materials Characterization

X-ray diffraction (XRD, Empyrean 2) was employed to characterize the structural evolution in the range of $5\text{--}80^\circ$ with a scan rate of 5° min^{-1} . Rietveld refinement experiments were determined by fullprof software to clarify the contents of NFP, NFPP and NFPO. The morphological information was revealed by scanning electron microscope (SEM, JEOL-JSM7900F) and transmission electron microscope (TEM, Titan, G2 60–300). The elemental distribution was carried out by energy dispersive X-ray spectroscopy (EDS) affiliated with TEM. Fourier Transform infrared spectroscopy (FT-IR, Nicolet 380, Thermo Nicolet Corporation) with KBr tablet was utilized to evaluate the surface interaction. Moreover, the coating carbon contents was determined by thermogravimetric analysis (TG STA300). The detailed bonding information of the as-prepared materials was revealed by X-ray photoelectron spectroscopy (XPS, ULVAC-PHI VersaProbe 4).

Electrochemical Tests

The working electrode was made by active materials, conductive agent (Super P) and binder (PVDF) in a mass ratio of 7:2:1. The mixture was milled absolutely to make a uniform slurry with the addition of N-methylpyrrolidone (NMP) based on the solid content of 27–35%. The smooth slurry was obtained by mixed for about 10 min at 200–1000 rpm. After that, the slurry was pasted onto an aluminum foil with the thickness of 100 μm and transferred into a vacuum oven at 90 °C for 12 h. And then, it was pouched into disks with diameters around 14 cm. The mass loading was controlled at $1.5\text{--}2.0 \text{ mg cm}^{-2}$. The 2025-type coin cells were assembled in an Ar-filled glove box which the contents of H_2O and O_2 were below 0.1 ppm. Typically, the sodium metal was used as counter electrode, glass fiber was employed as separator and 1 M NaClO_4 in PC (polypropylene ester) and EC (ethyl cellulose) (1:1 by volume) with 5 vol.% FEC additive (Fluoroethylene carbonate) was acted as electrolyte. After laying aside for 8 h, the as-assembled cells were used for further electrochemical tests. Galvanostatic charge/discharge and galvanostatic intermittent titration technique (GITT) measurements were conducted on Neware test system. Cyclic voltammetry test was carried out in CHI1000 C electrochemical station in a scan rate of 0.1 Mvs^{-1} . Electrochemical impedance spectroscopy (EIS) was obtained by Gamry Electrochemical System

in a frequency range of 0.1 kHz–100 kHz and fitted by Zview software. All the tests were performed at room temperature.

Acknowledgements

This work was supported by the National Science Foundation of China (51974370, 52122407, 52174285), the Science and Technology Innovation Program of Hunan Province (2022RC3048), Hunan Key Areas of R&D Plan (2022GK2049), Science and Technology Innovation Leading Plan of Hunan High-tech Industry (2022GK4054), the Natural Science Foundation for Young Scholars of Hunan Province (Project 2022JJ40599), the Natural Science Foundation for Distinguished Young Scholars of Hunan Province (No. 2024JJ2077).

Conflict of Interests

The authors declare that they have no known competing financial interests or personal relationships that could have appeared to influence the work reported in this paper.

Data Availability Statement

The data that support the findings of this study are available from the corresponding author upon reasonable request.

Keywords: Sodium-ion batteries • Cathode materials • $\text{Na}_4\text{Fe}_3(\text{PO}_4)_2\text{P}_2\text{O}_7 \cdot \text{NaFePO}_4 \cdot \text{Na}_2\text{FeP}_2\text{O}_7$

- [1] a) N. Sharmili, R. Nagi, P. Wang, *J. Energy Storage* **2023**, *68*, 107622; b) M. Şen, M. Özcan, Y.-R. Eker, *Next Sustainability* **2024**, *3*, 100036.
- [2] R. A. Rincón, G. Heydenrych, *Batter. Supercaps* **2018**, *1*, 3–5.
- [3] a) K. Chayambuka, G. Mulder, D. L. Danilov, P. H. L. Notten, *Adv. Energy Mater.* **2018**, *8*, 1800079; b) T. Perveen, M. Siddiq, N. Shahzad, R. Ihsan, A. Ahmad, M.-I. Shahzad, *Angew. Chem. Int. Ed.* **2020**, *119*, 109549; c) J.-Y. Hwang, S.-T. Myung, Y.-K. Sun, *Chem. Soc. Rev.* **2017**, *46*, 3529–3614; d) N. Wu, Z. Zhao, R. Hua, X. Wang, Y. Zhang, J. Li, G. Liu, D. Guo, G. Sun, X. Liu, J. Zhang, *Adv. Energy Mater.* **2024**, *14*, 2400371.
- [4] a) X. Li, X.-H. Ma, D. Su, L. Liu, R. Chisnell, S.-P. Ong, H. Chen, A. Toumar, J.-C. Idrobo, Y.-C. Lei, J.-M. Bai, F. Wang, J.-W. Lynn, Y.-S. Lee, G. Ceder, *Nat. Mater.* **2014**, *13*, 586–592; b) R. Berthelot, D. Carlier, C. Delmas, *Nat. Mater.* **2011**, *10*, 74–80; c) X.-H. Li, Y.-M. Fan, B. Johannessen, X. Xu, K.-W. See, W.-K. Pang, *Batter. Supercaps* **2024**, *7*, e202300618; d) X. Zhu, S.-W. Xu, X.-Z. Wang, M.-T. Liu, Y.-H. Cheng, P.-F. Wang, *Batter. Supercaps* **2023**, *6*, e202200473.
- [5] a) Y. Liu, Y. Qiao, W.-X. Zhang, Z. Li, X. Ji, L. Miao, L.-X. Yuan, X.-L. Hu, Y.-H. Huang, *Nano Energy* **2015**, *12*, 386–393; b) J.-F. Qian, C. Wu, Y.-L. Cao, Z.-F. Ma, Y.-H. Huang, X.-P. Ai, H.-X. Yang, *Adv. Energy Mater.* **2018**, *8*, 1702619; c) H.-Y. Fu, M.-Y. Xia, R.-J. Qi, X.-Q. Liang, M. Zhao, Z.-L. Zhang, X.-M. Lu, G.-Z. Cao, *J. Power Sources* **2018**, *399*, 42–48; d) S. Baumgart, M. Sotoudeh, A. Groß, *Batter. Supercaps* **2023**, *6*, e202300294.
- [6] a) F. Sanz, C. Parada, U. Amador, M.-A. Monge, C.-R. Valero, *J. Solid State Chem.* **1996**, *123*, 129–139; b) K. Jayanthi, S. Lochab, P. Barpanda, A. Navrotksy, *J. Phys. Chem. C* **2023**, *127*, 11700–11706; c) P.-R. Kumar, H.-B. Yahia, I. Belharouak, M.-T. Sougrati, S. Passerini, R. Amin, R. Essehli, *J. Solid State Electrochem.* **2020**, *24*, 17–24; d) H. Kim, I. Park, D.-H. Seo, S. Lee, S.-W. Kim, W. J. Kwon, Y.-U. Park, C. S. Kim, J. Seokwoo, K. Kang, *J. Am. Chem. Soc.* **2012**, *134*, 10369–10372; e) F. Sanz, C. Parada, J.-M. Rojo, C. Ruiz-Valero, *Chem. Mater.* **2001**, *13*, 1334–1340.
- [7] a) A. Gezović, M.-J. Vujković, M. Milović, V. Grudić, R. Dominko, S. Mentus, *Energy Storage Mater.* **2021**, *37*, 243–273; b) S. Ryu, J.-E. Wang, J.-H. Kim, R. Ruffo, Y.-H. Jung, D.-K. Kim, *J. Power Sources* **2019**, *444*, 227274; c) L.-B. Tang, X.-H. Liu, Z. Li, X.-M. Pu, J.-H. Zhang, Q.-J. Xu, H.-M. Liu, Y.-G. Wang, Y.-Y. Xia, *ACS Appl. Mater. Interfaces* **2019**, *11*, 27813–27822.
- [8] a) T.-C. Yuan, Y.-X. Wang, J.-X. Zhang, X.-J. Pu, X.-P. Ai, Z.-X. Chen, H.-X. Yang, Y.-L. Cao, *Nano Energy* **2019**, *56*, 160–168; b) X.-P. Li, Y. Meng, D. Xiao, *Chem. Eur. J.* **2023**, *29*, e202203381; c) X.-J. Pu, H.-M. Wang, T.-C. Yuan, S.-A. Cao, S.-Y. Liu, L. Xu, H.-X. Yang, X.-P. Ai, Z.-X. Chen, Y.-L. Cao, *Energy Storage Mater.* **2019**, *22*, 330–336; d) J.-H. Zhang, L.-B. Tang, Y. Zhang, X.-Q. Li, Q.-J. Xu, H.-M. Liu, Z.-F. Ma, *J. Power Sources* **2021**, *498*, 229907; e) X. Li, Y. Zhang, B. Zhang, K. Qin, H. Liu, Z.-F. Ma, *J. Power Sources* **2022**, *521*, 230922; f) F.-Y. Xiong, J.-T. Li, C.-L. Zuo, X.-L. Zhang, S.-S. Tan, Y.-L. Jiang, Q.-Y. An, P.-K. Chu, L.-Q. Mai, *Adv. Funct. Mater.* **2023**, *33*, 2211257.
- [9] a) S.-M. Wood, C. Eames, E. Kendrick, M.-S. Islam, *J. Phys. Chem. C* **2015**, *119*, 15935–15941; b) H. Kim, G. Yoon, I. Park, J. Hong, K.-Y. Park, J. Kim, K.-S. Lee, N.-E. Sung, S. Lee, K. Kang, *Chem. Mater.* **2016**, *28*, 7241–7249.
- [10] a) P. Barpanda, T. Ye, S.-I. Nishimura, S.-C. Chung, Y. Yamada, M. Okubo, H. Zhou, A. Yamada, *Electrochem. Commun.* **2012**, *24*, 116–119; b) N. V. Kosova, V. A. Belotserkovsky, *Electrochim. Acta* **2018**, *278*, 182–195.
- [11] a) H. Kim, I. Park, S. Lee, H. Kim, K.-Y. Park, Y.-U. Park, H. Kim, J. Kim, H.-D. Lim, W.-S. Yoon, K. Kang, *Chem. Mater.* **2013**, *25*, 3614–3622; b) N. V. Kosova, A. A. Shindrov, *Batteries* **2019**, *5*, 39; c) X.-D. Ma, Z.-Y. Pan, X.-H. Wu, P.-K. Shen, *Chem. Eng. J.* **2019**, *365*, 132–141; d) A. Zhao, T.-C. Yuan, P. Li, C. Liu, H.-J. Cong, X.-J. Pu, Z.-X. Chen, X.-P. Ai, H.-X. Yang, Y.-L. Cao, *Nano Energy* **2022**, *91*, 106680; e) A. Zhao, C.-Y. Liu, F.-J. Ji, S.-H. Zhang, H.-M. Fan, W.-H. Ni, Y.-J. Fang, X.-P. Ai, H.-X. Yang, Y.-L. Cao, *ACS Energy Lett.* **2023**, *8*, 753–761; f) N. Wang, R.-Q. Wang, M.-Q. Jiang, J.-X. Zhang, *J. Alloy Compd.* **2021**, *870*, 159382.
- [12] a) J. Kim, D.-H. Seo, H. Kim, I. Park, J.-K. Yoo, S.-K. Jung, Y.-U. Park, W. A. Goddard III, K. Kang, *Energy Environ. Sci.* **2015**, *8*, 540–545; b) R.-R. Kapaei, A.-A. Chekannikov, S.-A. Novikova, T.-L. Kulova, A.-M. Skundin, A.-B. Yaroslavtsev, *Mendeleev Commun.* **2017**, *27*, 263–264; c) H. Kim, R. A. Shakoor, C. Park, S. Y. Lim, J.-S. Kim, Y. N. Jo, W. Cho, K. Miyasaka, R. Kahraman, Y. Jung, J. W. Choi, *Adv. Funct. Mater.* **2013**, *23*, 1147–1155; d) X.-L. Liu, J.-D. Wang, M.-Y. Du, Q. Zhu, K. Robeyns, X.-Z. Zhang, V. Kumar, J.-F. Gohy, Y. Garcia, A. Vlad, *Batter. Supercaps* **2022**, *5*, e202100390.
- [13] W.-B. Fei, Y.-A. Wang, X.-P. Zhang, J.-X. Zhang, S.-X. Lu, K.-X. Rao, K.-Y. Sun, M.-T. Deng, Y.-X. Liu, Q.-Q. Li, L. Wu, Y.-L. Sui, *Chem. Eng. J.* **2024**, *493*, 152523.
- [14] J.-J. Song, J. Yang, M.-H. Alfaruqi, W. Park, S. Park, S. Kim, J. Jo, J. Kim, *J. Korean Chem. Soc.* **2016**, *53*, 406–410.
- [15] H. Zhang, Y.-J. Cao, Z.-L. Liu, X.-S. Cheng, X.-L. Li, J. Xu, N. Wang, H. Yang, Y. Liu, J.-X. Zhang, *ACS Sustainable Chem. Eng.* **2024**, *12*, 5310–5318.
- [16] a) S. Xing, J.-M. Zhao, Y. Li, X.-H. Sun, H.-Z. Liu, Y.-Z. Hu, *ACS Appl. Energy Mater.* **2015**, *127*, 10049–10054; b) R. Essehli, B. El Bali, S. Benmokhtar, H. Fuess, I. Svoboda, S. Obbade, *J. Alloy Compd.* **2010**, *493*, 654–660.
- [17] Y. You, A. Manthiram, *Adv. Energy Mater.* **2018**, *8*, 1701785.
- [18] J.-C. Zheng, B.-Y. Yang, X.-W. Wang, B. Zhang, H. Tong, W.-J. Yu, J.-F. Zhang, *ACS Sustainable Chem. Eng.* **2018**, *6*, 4966–4972.
- [19] a) H.-M. Dai, Y. Xu, Y. Wang, F.-Y. Cheng, Q. Wang, C. Fang, J.-T. Han, P.-K. Chu, *ACS Appl. Mater. Interfaces* **2024**, *16*, 7070–7079; b) Q.-D. Tao, H.-Y. Ding, X. Tang, K.-B. Zhang, J.-H. Teng, H.-M. Zhao, J. Li, *Energy Fuels* **2023**, *37*, 6230–6239; c) Y. Cao, C. Yang, Y. Liu, X. Xia, D. Zhao, Y. Cao, H. Yang, J. Zhang, J. Lu, Y. Xia, *ACS Energy Lett.* **2020**, *5*, 3788–3796; d) L.-M. Zhang, X.-D. He, S. Wang, N.-Q. Ren, J.-R. Wang, J.-M. Dong, F. Chen, Y.-X. Li, Z.-Y. Wen, C.-H. Chen, *ACS Appl. Mater. Interfaces* **2021**, *13*, 25972–25980; e) X.-C. Ge, H.-X. Li, J. Li, C.-H. Guan, X. Wang, L. He, S. Li, Y.-Q. Lai, Z.-A. Zhang, *Small* **2023**, *19*, 2302609; f) J.-Q. Gao, J.-Y. Zeng, W.-S. Jian, Y. Mei, L.-S. Ni, H.-J. Wang, K. Wang, X.-Y. Hu, W.-T. Deng, G.-Q. Zou, H.-S. Hou, X.-B. Ji, *Science Bull.* **2024**, *69*, 772–783; g) W. Ren, M.-L. Qin, Y.-F. Zhou, H. Zhou, J. Zhu, J.-A. Pan, J. Zhou, X.-X. Cao, S.-Q. Liang, *Energy Storage Mater.* **2023**, *54*, 776–783.

Manuscript received: June 30, 2024

Revised manuscript received: August 28, 2024

Version of record online: October 28, 2024